

How to Train Your Event Camera Neural Network

Timo Stoffregen^{*,1}, Cedric Scheerlinck^{*,2}, Davide Scaramuzza³, Tom Drummond¹,
Nick Barnes², Lindsay Kleeman¹, and Robert Mahony²

¹ Monash University, Melbourne, Australia

² Australian National University, Canberra, Australia

³ University of Zurich, Zurich, Switzerland

Abstract. Event cameras are paradigm-shifting novel sensors that report asynchronous, per-pixel brightness changes called ‘events’ with unparalleled low latency. This makes them ideal for high speed, high dynamic range scenes where conventional cameras would fail. Recent work has demonstrated impressive results using Convolutional Neural Networks (CNNs) for video reconstruction and optic flow with events. We present strategies for improving training data for event based CNNs that result in 25-40 % boost in performance of existing state-of-the-art (SOTA) video reconstruction networks retrained with our method, and up to 80 % for optic flow networks. A challenge in evaluating event based video reconstruction is lack of quality groundtruth images in existing datasets. To address this, we present a new **High Quality Frames (HQF)** dataset, containing events and groundtruth frames from a DAVIS240C that are well-exposed and minimally motion-blurred. We evaluate our method on HQF + several existing major event camera datasets.

Video, code and datasets: <https://timostoff.github.io/20ecnn>

1 Introduction

Event-based cameras such as the Dynamic Vision Sensor (DVS) [18] are novel, bio-inspired visual sensors. Presenting a paradigm-shift in visual data acquisition, pixels in an event camera operate by asynchronously and independently reporting intensity changes in the form of events, represented as a tuple of x, y location, timestamp t and polarity of the intensity change s . By moving away from fixed frame-rate sampling of conventional cameras, event cameras deliver several key advantages in terms of low power usage (in the region of 5 mW), high dynamic range (140 dB), low latency and timestamps with resolution on the order of μ s.

With the recent preponderance of deep learning techniques in computer vision, the question of how to apply this technology to event data has been the subject of several recent works. Zhu *et al.* [44] propose an unsupervised network able to learn optic flow

* Equal contribution.

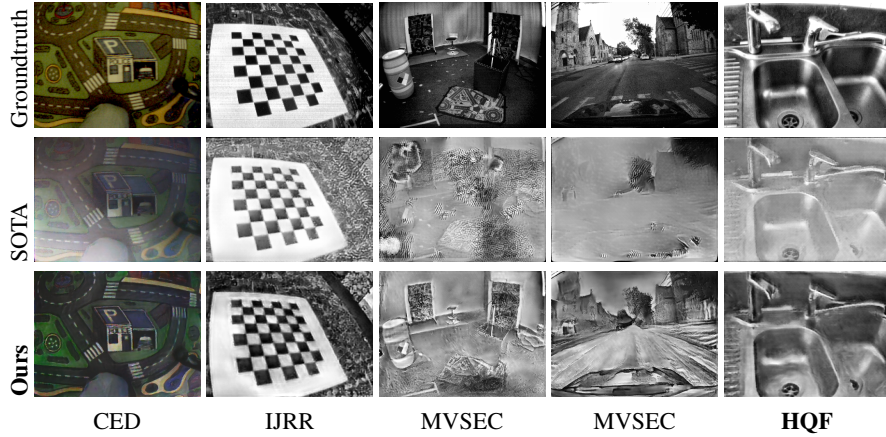


Fig. 1: Top: groundtruth reference image. Middle/bottom: state-of-the-art E2VID [28] vs. our reconstructed images from events only. Challenging scenes from event camera datasets: CED [34], IJRR [23], MVSEC [43] and our **HQF** dataset.

from real event data, while Rebecq *et al.* [27] showed that supervised networks trained on synthetic events transferred well to real event data. Simulation shows promise since data acquisition and groundtruth are easily obtainable, in contrast to using real data. However, mismatch between synthetic and real data degrades performance, so a key challenge is simulating realistic data.

We generate training data that better matches real event camera data by analysing the statistics of existing datasets to inform our choice of simulation parameters. A major finding is that the contrast threshold (CT) - the minimum change in brightness required to trigger an event - is a key simulation parameter that impacts performance of supervised CNNs. Further, we observe that the apparent contrast threshold of real event cameras varies greatly, even within one dataset. Previous works such as event based video reconstruction [29] choose contrast thresholds that work well for some datasets, but fail on others. Unsupervised networks trained on real data such as event based optic flow [44] may be retrained to match any real event camera - at the cost of new data collection and training. We show that using CT values for synthetic training data that are correctly matched to CTs of real datasets is a key driver in improving performance of retrained event based video reconstruction and optic flow networks across multiple datasets. In addition, we propose a simple noise model that can be used to dynamically augment event data at train time, and retrain with a variety of augmentation parameters to elucidate their effects, yielding up to 10 % improvement vs. unaugmented.

A challenge in evaluating image and video reconstruction from events is lack of quality groundtruth images registered and time-synchronized to events, because most existing datasets focus on scenarios where event cameras excel (high speed, HDR) and conventional cameras fail. To address this limitation, we introduce a new High Quality Frames (HDF) dataset that provides several sequences in well lit environments with minimal motion blur. These sequences are recorded with a DAVIS240C event camera

that provides perfectly aligned frames from an integrated Active Pixel Sensor (APS). HQF also contains a diverse range of motions and scene types, including slow motion and pauses that are challenging for event based video reconstruction. We quantitatively evaluate our method on two major event camera datasets: IJRR [23] and MVSEC [43], in addition to our HQF, demonstrating gains of 25-40 % for video reconstruction and up to 80 % for optic flow when we retrain existing SOTA networks.

Contribution We present a method to generate synthetic training data that improves generalizability to real event data, guided by statistical analysis of existing datasets. We additionally propose a simple method for dynamic train-time noise augmentation that yields up to 10 % improvement for video reconstruction. Using our method, we retrain several network architectures from previously published works on video reconstruction [29, 33] and optic flow [44, 45] from events. We are able to show significant improvements that persist over architectures and tasks. Thus, we believe our findings will provide invaluable insight for others who wish to train models on synthetic events for a variety of tasks. We provide a new comprehensive High Quality Frames dataset targeting groundtruth image frames for video reconstruction evaluation. Finally, we provide our data generation code, training set, training code and our pretrained models, together with dozens of useful helper scripts for the analysis of event-based datasets to make this task easier for fellow researchers.

In summary, our major contributions are:

- A method for simulating training data that yields 25-40 % and up to 80 % improvement for event based video reconstruction and optic flow CNNs.
- Dynamic train-time noise augmentation.
- A novel High Quality Frames dataset.
- Extensive evaluation and ablation of our method.
- Open-source code, training data and pretrained models.

The remainder of the paper is as follows. Section 2 reviews related works. Section 3 outlines our method for generating training data, training and evaluation, and introduces our HQF dataset. Section 4 presents experimental results on video reconstruction, optic flow and ablation studies. Section 5 discusses our major findings and concludes the paper.

2 Related Works

2.1 Video Reconstruction

Video and image reconstruction from events has been a popular topic in the event based vision literature. Several approaches have been proposed in recent years; [14] *et al.* used an EKF to reconstruct images from a rotating event camera, later extending this approach to full 6-DOF camera motions [15]. Bardow *et al.* [2] used a sliding spatiotemporal window of events to simultaneously optimize both optic flow and intensity estimates using the primal-dual algorithm, although this method remains sensitive to hyperparameters. Recently Scheerlinck *et al.* [31, 32] achieved computationally efficient, temporally continuous video reconstruction via direct integration through a high-pass

filter. This approach can be combined with conventional frames, if available, to provide low frequency components of the image. However, if taken alone, this approach suffers from artifacts, such as ghosting effects and bleeding edges due to imbalances in the contrast thresholds of the generated events. Reinbacher *et al.* [30] used manifold regularization of events integrated over time into a surface of active events (SAE [22]) to reconstruct video from events.

More recently, CNNs have been bought to bear on the problem of video reconstruction. Rebecq *et al.* [27] presented a recurrent network architecture, which took events, discretized into a voxel grid representation and the last k output images as inputs to generate the next frame. This work was updated in [29] where an LSTM was introduced to replace the simpler method of reusing previous frames. Further, a temporal consistency loss based on [16] was introduced to reduce flickering artifacts in the video, due to small differences in the reconstruction of subsequent frames. This work is the current state-of-the-art. Scheerlinck *et al.* were able to reduce the model complexity by 99 % with the *FireNet* architecture [33], with only minor trade-offs in reconstruction quality, to allow for high frequency inference.

2.2 Optic Flow

Since event based cameras are considered a good fit for applications involving motion [8], much work has been done on estimating optic flow with event cameras [1–4, 6, 10, 20, 36, 37]. More recently however, Zhu *et al.* proposed a CNN for estimating optic flow from events [44], together with the Multi-Vehicle Stereo Event Camera (MVSEC) dataset, which contained ground truth optic flow estimated from depth and ego-motion sensors. This network formed 4-channel images from the events by recording event counts and the most recent timestamps for negative and positive events. The loss imposed on this network was an image-warping loss [13], which used the flow to register subsequent APS frames from the DAVIS event camera and used the photometric loss as the training signal. A similar approach was taken by Ye *et al.* [40], in a network that estimated depth and camera pose to calculate optic flow. Finally, Zhu *et al.* improved on prior work by replacing the image-warping loss with an event-warping loss, which directly transports events to a reference time using the flow estimates. We use this method to evaluate optic flow results in our network (see Sec. 4.2). They also introduced a novel event discretization as the input representation, in which events are placed into bins with temporal bilinear interpolation to produce a voxel grid. All of these networks, however, trained on data from MVSEC [43] and [40] even validated and trained on the same sequences; our results (Sec. 4.2) indicate that as a result, these networks suffer from overfitting.

2.3 Input Representations

Asynchronous spiking neural networks are theoretically capable of natively processing spatiotemporal data such as an event stream. While they have been applied to event cameras for tasks such as object recognition [17, 24, 25] or even optic flow prediction [3, 4], the lack of appropriate hardware or effective error backpropagation techniques renders them yet uncompetitive with state-of-the-art CNNs or even hand-crafted

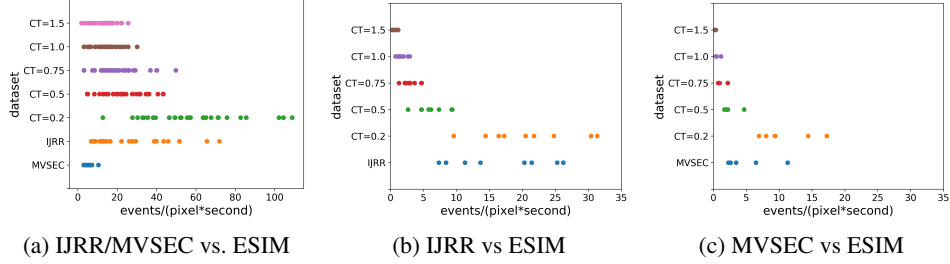


Fig. 2: Each dot represents a sequence from the given dataset (y-axis). (a) $\frac{\text{events}}{\text{pix}\cdot\text{s}}$ of IJRR and MVSEC vs. ESIM training datasets (CT 0.2-1.5) described in Section 3.2. (b) $\frac{\text{events}}{\text{pix}\cdot\text{s}}$ of IJRR vs. ESIM events simulated from IJRR *APS frames*. (c) $\frac{\text{events}}{\text{pix}\cdot\text{s}}$ of MVSEC vs. ESIM events simulated from MVSEC *APS frames*.

methods. However, in order to train CNNs with events, the events must first be transformed into an amenable grid-based representation. Many different input representations have been proposed, from simple event images [21, 44] (where events are accumulated along the temporal dimension to form a frame), SAE [44] (where the latest timestamp is recorded at each pixel), Histogram of Active Events [35] (HATS, where events are transformed into histograms of averaged time surfaces) and even learned input representations, where events are sampled into a grid using convolutional kernels. However, Rebecq *et al.* [29] and Zhu *et al.* [45] found best results using voxel grid representations of the events, in which the temporal dimensions of the events is essentially discretized and subsequently binned into an n dimensional grid.

3 Method

3.1 Event Camera Contrast Threshold

In an ideal event camera, a pixel at (u, v) triggers an event e_i at time t_i when the brightness since the last event e_{i-1} at that pixel changes by a threshold C , given $t - t_{i-1} < r_f$, the refractory period of that pixel. C is referred to as the contrast threshold (CT) and can be typically adjusted in modern event cameras. In reality, the values for C are not constant in time nor homogeneous over the image plane nor is the positive threshold C_p necessarily equal to the negative threshold C_n . In simulation (e.g. using ESIM [26]), CTs are typically sampled from $\mathcal{N}(\mu=0.18, \sigma=0.03)$ to model this variation [12, 27, 29]. The CT is an important simulator parameter since it determines the number and distribution of events generated from a given scene.

While the real CTs of previously published datasets are unknown, one method to estimate CTs is via the proxy measurement of average events per pixel per second ($\frac{\text{events}}{\text{pix}\cdot\text{s}}$). Intuitively, higher CTs tend to reduce the $\frac{\text{events}}{\text{pix}\cdot\text{s}}$ for a given scene. While other methods of CT estimation exist (see supp. material), we found that tuning the simulator CTs to match $\frac{\text{events}}{\text{pix}\cdot\text{s}}$ of real data worked well. Since this measure is affected by scene dynamics

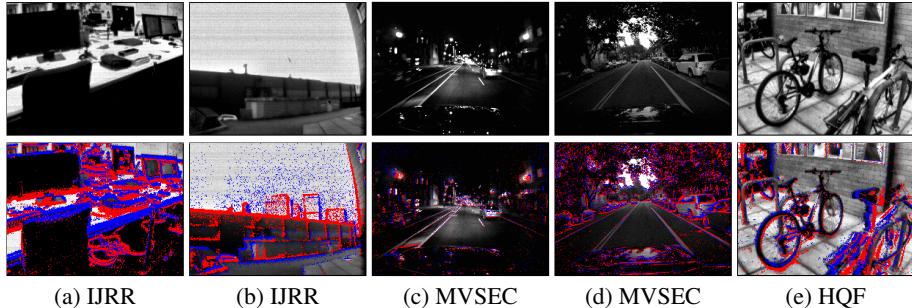


Fig. 3: Note that in many sequences from the commonly used IJRR and MVSEC datasets, the accompanying APS frames are of low quality. The top row shows the APS frames, the bottom row overlays the events. As can be seen, many features are not visible in the APS frames, making quantitative evaluation difficult. This motivates our own High Quality Frames dataset (HQF).

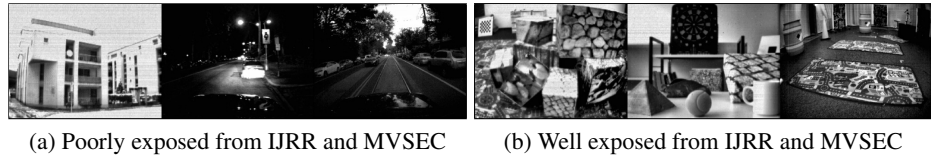


Fig. 4: Examples of frames from IJRR and MVSEC after local histogram equalization, with poorly exposed sequences in 4a, and better exposed images in 4b.

(i.e. faster motions increase $\frac{\text{events}}{\text{pix}\cdot\text{s}}$ independently of CT), we generated a diverse variety of realistic scene dynamics. The result of this experiment (Fig. 2a) indicates that a contrast threshold setting of between 0.2 and 0.5 would be more appropriate for IJRR sequences. The larger diversity of motions is also apparent in the large spread of the $\frac{\text{events}}{\text{pix}\cdot\text{s}}$ over the sequences, compared to MVSEC whose sequences are tightly clustered.

As an alternative experiment to determine CTs of existing datasets, we measured the $\frac{\text{events}}{\text{pix}\cdot\text{s}}$ of events simulated using the actual APS (groundtruth) frames of IJRR and MVSEC sequences. Given high quality images with minimal motion blur and little displacement, events can be simulated through image interpolation and subtraction. Given an ideal image sequence, the simulator settings should be tunable to get the exact same $\frac{\text{events}}{\text{pix}\cdot\text{s}}$ from simulation as from the real sensor. Unfortunately APS frames are not usually of a very high quality (Fig. 3), so we were limited to using this approach on carefully curated snippets (Fig. 4). The results of this experiment in Fig. 2b and 2c indicate similar results of lower contrast thresholds for IJRR and higher for MVSEC, although accuracy is limited by the poor quality APS frames.

3.2 Training Data

We use an event camera simulator, ESIM [26] to generate training sequences for our network. There are several modes of simulation available, of which we use ‘‘Multi-Object-2D’’, which facilitates moving images in simple 2D motions, restricted to translations, rotations and dilations over a planar background. This generates sequences reminiscent of Flying Chairs [7], where objects move across the screen at varying velocities. In our generation scheme, we randomly select images from COCO [19], which receive random trajectories over the image plane. Our dataset contains 280 sequences, 10 s in length. Sequences alternate between four archetypical scenes; slow motion with 0-5 foreground objects, medium speed motion with 5-10 foreground objects, fast speed with 5-20 foreground objects and finally, full variety of motions with 10-30 foreground objects. This variety allows models trained on our dataset to generalize well to arbitrary real world camera motions, since the network has seen a wide range of scene dynamics. Sequences are generated with contrast thresholds (CTs) between 0.1 and 1.5 in ascending order. Since real event cameras do not usually have perfectly balanced positive and negative thresholds, the positive threshold $C_p = C_n \cdot x$, $x \in \mathcal{N}(\mu=1.0, \sigma=0.1)$.

The events thus generated are discretized into a voxel grid representation. In order to ensure synchronicity with the ground truth frames of our training set and later with the ground truth frames of our validation set, we always take all events between two frames to generate a voxel grid. Given N events $e_i = \{x_i, y_i, t_i, p_i\}_{i=0, \dots, N}$ spanning $\Delta_T = t_N - t_0$ seconds, a voxel grid V with B bins can be formed through temporal bilinear interpolation via

$$V_{k \in [0, B-1]} = \sum_{i=0}^N p_i \max(0, 1 - |t_i^* - k|) \quad (1)$$

where t_i^* is the timestamp normalized to the range $[0, B - 1]$ via $t_i^* = \frac{t_i - t_0}{\Delta_T} (B - 1)$ and the bins are evenly spaced over the range $[t_0, t_N]$. This method of forming voxels has some limitations; it is easy to see that the density of the voxels can vary greatly, depending on the camera motion and frame rate of the camera. This makes it important to show the network a dataset with varying numbers of events generated, so that it sees a large variety of voxel densities. During inference, other strategies of voxel generation can be employed, as further discussed in the supplementary materials. We use $B = 5$ throughout the experiments in the paper. In earlier experiments we found values of $B = 2, 5, 15$ to produce no significant differences.

3.3 Sequence Length

To train recurrent networks, we sequentially passed L inputs to the network and computed the loss for each output. Finally, the losses are summed and a backpropagation update is performed based on the gradient of the final loss with respect to the network weights. Since the recurrent units in the network are initialized to zero, lower values of L restrict the temporal support that the recurrent units see at train time. To investigate the impact of sequence length L , we retrain our networks using $L = 40$ (as in E2VID [29]) and $L = 120$. In the case of non-recurrent networks such as EV-FlowNet [44, 45], we ignore the sequence length parameter.

3.4 Loss

For our primary video reconstruction loss function we used ‘‘learned perceptual image patch similarity’’ (LPIPS) [42]. LPIPS is a fully differentiable similarity metric between two images that compares hidden layer activations of a pretrained network (e.g. Alex-Net or VGG), and is shown to better match human judgement of image similarity than photometric error and SSIM [39]. Since our event tensors are synchronized to the groundtruth image frames by design (the final event in the tensor matches the frame timestamp), we compute the LPIPS distance between our reconstruction and the corresponding groundtruth frame. As recommended by the authors [42], we use the Alex-Net variant of LPIPS. We additionally impose a temporal consistency loss [16] that measures photometric error between consecutive images after registration based on optic flow, subject to an occlusion mask. For optic flow, we use the L1 distance between our prediction and groundtruth as the training loss.

3.5 Data Augmentation

During training, Rebecq *et al.* [29] occasionally set the input events to zero and perform a forward-pass step within a sequence, using the previous groundtruth image frame to compute the loss. The probability of initiating a pause when the sequence is running $P(p|r) = 0.05$, while the probability of maintaining the paused state when the sequence is already paused $P(p|p) = 0.9$ to encourage occasional long pauses. This encourages the recurrent units of the network to learn to ‘preserve’ the output image in absence of new events. We retrain our network with and without pauses to investigate the impact of pause augmentation (Tab. 5).

Event cameras provide a noisy measurement of brightness change, subject to background noise, refractory period after an event and hot pixels that fire many spurious events. To simulate real event data, we applied a refractory period of 1ms. At train time, for each sequence of L input event tensors we optionally add zero-mean Gaussian noise ($\mathcal{N}(\mu=0, \sigma=0.1)$) to the event tensor to simulate uncorrelated background noise, and randomly elect a few ‘hot’ pixels. The number of hot pixels is drawn from a uniform distribution from 0 to 0.0001, multiplied by the total number of pixels. Hot pixels have a random value ($\mathcal{N}(\mu=0, \sigma=0.1)$) added to every temporal bin in each event tensor within a sequence. To determine whether augmenting the training data with noise benefits performance on real data, we retrain multiple models with various noise parameters (Tab. 5).

3.6 Architecture

To isolate the impact of our method from choice of network architecture, we retrain state-of-the-art (SOTA) video reconstruction network E2Vid [29] and the SOTA optic flow network described in [44, 45]. Thus, differences in performance for each task are not due to architecture. Additionally, we aim to show that our method generalizes to multiple architectures. While we believe architecture search may further improve results, it is outside the scope of this paper.

Table 1: Breakdown of the sequences included in HQF. To provide some inter-device variability, the dataset is taken with two separate DAVIS 240C cameras, 1 and 2.

Sequence	Length	Cam	#Frames	#Events	Description
bike_bay_hdr	99.0	1	2431	19763043	Camera moves from dim to bright
boxes	24.2	1	540	10050781	Indoor light, translations
desk	65.8	2	1491	13516351	Natural light, various motions
desk_fast	32.0	2	724	12622934	Natural light, fast motions
desk_hand_only	20.6	2	467	777177	Indoor light, static camera
desk_slow	63.3	2	1434	1926605	Natural light, slow motions
engineering_posters	60.7	1	1267	15376272	Indoor light, text and images
high_texture_plants	43.2	1	1090	14602389	Outdoors, high textures
poster_pillar_1	41.8	1	998	7056573	Outdoors, text and images
poster_pillar_2	25.4	1	613	2540922	Outdoors, text and images, long pause
reflective_materials	28.9	1	619	7753856	Natural light, reflective objects
slow_and_fast_desk	75.6	1	1744	15030414	Natural light, diverse motion
slow_hand	38.9	1	901	7635825	Indoor, slow motion, static camera
still_life	68.1	1	1194	42740481	Indoors, Indoor light, 6DOF motions

3.7 High Quality Frames Dataset

To evaluate event camera image reconstruction methods, we compare reconstructed images to temporally synchronized, registered groundtruth reference images. Event cameras such as the DAVIS [5] can capture image frames (in addition to events) that are timestamped and registered to the events, that may serve as groundtruth. Previous event camera datasets such as IJRR [23] and MVSEC [43] contain limited high quality DAVIS frames, while many frames are motion-blurred and or under/overexposed (Fig. 3). As a result, E2VID [29] manually rejected poor quality frames, evaluating on a smaller subset of IJRR.

We collect and present a new High Quality Frames dataset (HQB) aimed at providing groundtruth DAVIS frames that are minimally motion-blurred and well exposed. In addition, our HQF covers a wider range of motions and scene types than the evaluation dataset used for E2VID, including: static/dynamic camera motion vs. dynamic camera only, very slow to fast vs. medium to fast and indoor/outdoor vs. indoor only. To record HQF, we used two different DAVIS240C sensors to capture data with different noise/CT characteristics. We used default bias settings loaded by the RPG DVS ROS driver⁴, and set exposure to either auto or fixed to maximize frame quality. Our HQF provides temporally synchronized, registered events and DAVIS frames.

4 Experiments

4.1 Contrast Thresholds

We investigate the impact of simulator CT parameter (see Sec. 3.1) by retraining several networks on simulated datasets with CTs ranging from 0.2 to 1.5. Each dataset contained the same sequences, differing only in CT. Table 2 shows that for reconstruction (evaluated on LPIPS), IJRR is best on a lower CT ≈ 0.2 , while MVSEC is best on

⁴ https://github.com/uzh-rpg/rpg_dvs_ros

Table 2: Evaluation of networks trained on simulated datasets with a variety of CTs from 0.2 to 1.5. ‘All’ is a dataset containing the full range of CTs from 0.2 to 1.5. Each network is evaluated for perceptual loss (LPIPS) and structural similarity (SSIM) on the real datasets IJRR, MVSEC and HQF after training for 200 epochs. Best in bold, runner-up in italics, in case of draw, winner taken from further truncated decimal places.

CT	IJRR			MVSEC			HQF			
	MSE	SSIM	LPIPS	MSE	SSIM	LPIPS	MSE	SSIM	LPIPS	
Reconstruction	0.20	0.04	0.60	0.25	0.10	0.35	0.55	0.05	0.50	0.38
	0.50	0.04	0.57	0.27	<i>0.10</i>	0.31	0.52	0.04	<i>0.51</i>	0.36
	0.75	0.05	0.56	0.28	0.11	0.29	0.53	0.05	0.51	0.36
	1.00	0.05	0.53	0.29	0.12	0.27	<i>0.51</i>	0.05	0.48	0.36
	1.50	0.06	0.52	0.30	0.09	0.30	0.52	0.05	0.47	0.38
	All	0.04	0.59	0.27	0.08	0.34	0.51	0.05	0.50	0.36
Optic Flow		FWL			FWL			FWL		
	0.2		4.12			0.14			0.89	
	0.5		4.02			0.14			0.89	
	0.75		4.18			0.14			0.89	
	1.0		3.93			0.14			0.88	
	1.5		3.70			0.14			0.86	
all			4.53			0.14			0.92	

high CT ≈ 1.0 . Interestingly, best or runner up performance is achieved when a wide range of CTs is used, indicating that exposing a network to additional event statistics outside the inference domain is not harmful, and may be beneficial. We also believe that a symptom of training with low CTs (thus higher $\frac{\text{events}}{\text{pix}\cdot\text{s}}$) is a loss of dynamic range in the output images. This occurs because the network, trained using many events, receives only few at inference, thus narrowing the range of output values. When training the original E2Vid network, dynamic range increases with CTs (see Tab. 3).

Table 3: Comparison of the dynamic range of reconstructed IJRR images from vanilla E2Vid and E2Vid trained on simulated datasets over a range of CTs. The range row shows the range of the 90th percentile - 10th percentile of the pixel values of the reconstructed images. For reference, E2Vid was trained on CTs of ≈ 0.18 .

Network	CT=0.2	CT=0.5	CT=0.75	CT=1.0	CT=1.5	CT=all	E2Vid
Range	89.2	103.7	105.9	104.8	100.0	103.3	77.3

Table 4: Comparison of various methods to optic flow estimated from Lidar depth and ego-motion sensors [43]. The average-endpoint-error to the Lidar estimate (AEE) and the percentage of pixels with EE above 3 and 5 % of the magnitude of the flow vector (%Outlier) are presented for each method (lower is better, best in bold). Zeros is the baseline error resulting from always estimating zero flow.

Dataset	outdoor_day1		outdoor_day2		indoor_flying1		indoor_flying2		indoor_flying3	
	AEE	%Outlier	AEE	%Outlier	AEE	%Outlier	AEE	%Outlier	AEE	%Outlier
Zeros	4.31	0.39	1.07	0.91	1.10	1.00	1.74	0.89	1.50	0.94
EVFlow [44]	0.49	0.20	-	-	1.03	2.20	1.72	15.10	1.53	11.90
Ours	1.40	0.95	4.19	0.49	1.30	0.97	2.31	0.72	1.81	0.82
ECN* [40]	0.35	0.04	-	-	0.21	0.01	-	-	-	-

*ECN is trained on 80 % of the sequence and evaluated on the remaining 20 %. This prevents direct comparison, however we include their result for completeness sake.

4.2 Evaluation

We evaluate our method by retraining two state-of-the-art event camera neural networks: E2VID [27, 29], and EV-FlowNet [44, 45]. We show that our method outperforms previous state-of-the-art in image reconstruction and optic flow on several publicly available event camera datasets including IJRR [23] and MVSEC [43], and our new High Quality Frames dataset (table 6).

For video reconstruction on the datasets HQF, IJRR and MVSEC (Tab. 6) we obtain a 40 %, 25 % and 35 % improvement over E2VID [29] respectively, using LPIPS. For HQF/IJRR we obtain a 20 % and 80 % improvement over EV-FlowNet [44] on FWL for optic flow, while performing slightly worse on MVSEC. Notably, EV-FlowNet was trained on MVSEC data (outdoor_day2 sequence), while ours was trained entirely on synthetic data, demonstrating the ability of our method to generalize well across different event data.

Image As in [29] we compare our reconstructed images to groundtruth (DAVIS frames) on three metrics; mean squared error (MSE), structural similarity [39] (SSIM) and perceptual loss [41] (LPIPS) which uses distance in the latent space of a pretrained deep network to quantify image similarity.

Since many of these datasets show scenes which are challenging for conventional cameras, we carefully selected sections of those sequences in which the frames appeared to be of higher quality (less blurred, better exposure etc). The exact cut times of the IJRR and MVSEC sequences can be found in the supplementary materials. However, we were also ultimately motivated to record our own dataset of high quality frames (HQP), which is further described above, of which we evaluated the entire sequence.

Flow In the absence of ground truth optic flow with which to compare, we use a warping loss [11] as a proxy measure of prediction accuracy (referred to henceforth as flow

warping loss, FWL). Essentially, the events $(x_i, y_i, t_i, s_{i=1,\dots,N})$ can be propagated by a per-pixel optical flow $u(x_i, y_i), v(x_i, y_i)$ to a reference time t' via

$$\begin{pmatrix} x'_i \\ y'_i \end{pmatrix} = \begin{pmatrix} x_i \\ y_i \end{pmatrix} + (t' - t_i) \begin{pmatrix} u(x_i, y_i) \\ v(x_i, y_i) \end{pmatrix}. \quad (2)$$

The resulting image (image of warped events, I) that is produced when these propagated events are assembled, becomes sharper if the flow is correct, as events are motion compensated. This sharpness can be evaluated using the variance of the image $\sigma^2(I)$ [9, 38], where a higher value indicates a better flow estimate. This measure of optic flow quality allows us to evaluate all sequences without a requirement for ground truth, although our networks are always trained with ground truth flow. Critically, using ground truth as the training signal allows our network to estimate dense flow, generating estimates even in regions with few or no events as opposed to using a warping loss directly as a training signal as in [45].

It is worth briefly mentioning the results in Tab. 4; the MVSEC dataset provides optic flow estimates computed from Lidar depth and ego motion sensors as a ground truth. This allows us to evaluate on average endpoint error (AEE) to this dataset. Our model performs slightly worse on AEE, however we feel it may be an unreliable metric (e.g. compared to FWL) given the inherent uncertainty of the Lidar and ego motion estimates (for example, given an estimate of zero flow, AEE returns a low (good) value (Tab. 4), whereas FWL worsens). Since we compute dense flow, we do not mask our flow by accumulated events for Tab. 4.

4.3 Ablation Study

To determine the impact of sequence length, noise and pause augmentation during training, we retrained E2VID architecture using sequence length 40 (L40) and 120 (L120), with and without noise + pause augmentation (NP) 5. Increasing sequence length from 40 to 120 did not improve our results. Adding noise and pause augmentation during training improved performance of L40 models by $\sim 5\text{-}10\%$, while giving mixed results on different datasets for L120 models. Qualitatively, adding more noise encourage the network to smooth more heavily, while less noise may encourage the network to ‘reconstruct’ noise events, resulting in artifacts (Fig. 1) observable in E2VID [29] (trained without noise).

5 Discussion

The significant improvements gained by training models on our synthetic dataset exemplify why it is important to try and minimize the gap between real and simulated events in both the event rate induced by varying the contrast thresholds and the dynamics of the simulation scenes. Our results are quite clear on this, with consistent improvements across tasks (reconstruction and optic flow) and architectures (deep recurrent networks like E2Vid, and U-Net based flow estimators) of up to 50 %. We believe this highlights the importance for researchers to pay attention to the properties of the events they are training on; are the settings of the camera or simulator such that they are generating

Table 5: Mean LPIPS [42] on our HQF dataset, IJRR [23] and MVSEC [43], for various training hyperparameter configurations. E2VID architecture retrained from scratch in all experiments. Key: L40/L120=sequence length 40/120, NP=noise and pause augmentation during training.

Model	HQF			IJRR			MVSEC		
	MSE	SSIM	LPIPS	MSE	SSIM	LPIPS	MSE	SSIM	LPIPS
L40NP	0.034	0.575	0.260	0.039	0.601	0.267	0.101	0.358	0.451
L40	0.039	0.547	0.305	0.041	0.593	0.277	0.100	0.346	0.473
L120NP	0.036	0.545	0.295	0.043	0.580	0.284	0.092	0.343	0.475
L120	0.038	0.541	0.317	0.040	0.599	0.281	0.085	0.359	0.502

more or less events? Are the scenes they are recording representative of the wide range of scenes that are likely to be encountered during inference?

In particular, it seems that previous works have inadvertently overfit their models to the events found in the chosen target dataset. Strong evidence of this can be seen in the results table 6 in the comparison between EVFlowNet and Ours. While the original EVFlowNet [45] is able to beat our network on the same dataset it was trained on (MVSEC), our network is much stronger on HQF and IJRR. It is also noticeable that EVFlowNet performs much better on sequences which are similar in dynamics to the slow, steady scenes found in MVSEC, examples being `slider_depth` and `calibration` from IJRR or `slow_hand` and `desk_slow` from HQF where it is almost on par with ours. For researchers looking to use an off-the-shelf pretrained network, our model may be a better fit, since it applies for a greater variety of sensors and scenes.

Similarly, our results speak for themselves on image reconstruction. While we outperform E2VID [29] on all datasets, the smallest gap is on IJRR, the dataset we found to have lower CTs. E2VID performs worst on MVSEC that contains higher CTs, consistent with our finding that performance is driven by similarity between training and evaluation event data.

In conclusion, future networks trained with synthetic data from ESIM or other simulators should take care to ensure the statistics of their synthetic data match the final use-case, using large ranges of CT values and appropriate noise and pause augmentation in order to ensure generalized models.

Acknowledgements

This work was supported by the Australian Government Research Training Program Scholarship and the Australian Research Council through the “Australian Centre of Excellence for Robotic Vision” under Grant CE140100016.

Table 6: Comparison of state-of-the-art methods of video reconstruction and optic flow to networks trained using our dataset on HQF, IJRR and MVSEC. Best in bold.

Dataset	MSE		SSIM		LPIPS		FWL	
	E2VID	Ours	E2VID	Ours	E2VID	Ours	EVFlow	Ours
HQF								
bike_bay_hdr	0.15	0.03	0.39	0.49	0.50	0.31	0.32	0.33
boxes	0.08	0.04	0.49	0.59	0.35	0.24	1.14	1.29
desk	0.14	0.03	0.51	0.60	0.37	0.22	0.52	0.62
desk_fast	0.09	0.03	0.55	0.61	0.37	0.24	1.55	1.87
desk_hand_only	0.12	0.04	0.54	0.58	0.62	0.36	0.07	0.09
desk_slow	0.13	0.04	0.55	0.63	0.42	0.24	0.06	0.07
engineering_posters	0.14	0.03	0.45	0.57	0.43	0.27	0.51	0.60
high_texture_plants	0.19	0.03	0.33	0.66	0.39	0.13	0.63	0.79
poster_pillar_1	0.15	0.03	0.38	0.49	0.52	0.26	0.23	0.30
poster_pillar_2	0.12	0.04	0.42	0.45	0.52	0.27	0.12	0.17
reflective_materials	0.13	0.03	0.44	0.56	0.44	0.28	0.61	0.71
slow_and_fast_desk	0.13	0.03	0.50	0.62	0.41	0.24	0.55	0.76
slow_hand	0.17	0.04	0.42	0.56	0.55	0.30	0.61	0.73
still_life	0.07	0.03	0.51	0.62	0.34	0.22	3.72	4.40
Mean	0.14	0.03	0.46	0.57	0.45	0.26	0.76	0.91
IJRR								
boxes_6dof	0.11	0.05	0.37	0.57	0.53	0.30	4.70	9.26
calibration	0.07	0.04	0.61	0.60	0.26	0.19	0.66	0.72
dynamic_6dof	0.12	0.06	0.43	0.47	0.41	0.34	2.42	4.18
office_zigzag	0.04	0.03	0.52	0.54	0.29	0.24	1.57	1.96
poster_6dof	0.07	0.04	0.49	0.60	0.41	0.26	5.12	9.79
shapes_6dof	0.03	0.02	0.79	0.76	0.28	0.24	0.88	2.12
slider_depth	0.10	0.03	0.54	0.64	0.33	0.20	0.71	0.74
Mean	0.08	0.04	0.54	0.60	0.37	0.27	2.29	4.11
MVSEC								
indoor_flying1	0.20	0.09	0.18	0.37	0.75	0.45	0.06	0.06
indoor_flying2	0.25	0.09	0.20	0.36	0.75	0.44	0.11	0.12
indoor_flying3	0.22	0.09	0.19	0.37	0.75	0.44	0.09	0.08
indoor_flying4	0.11	0.08	0.27	0.36	0.68	0.46	0.24	0.27
outdoor_day1	0.40	0.16	0.23	0.28	0.71	0.56	0.19	0.12
outdoor.day2*	0.14	0.10	0.36	0.37	0.62	0.42	0.28	0.15
Mean	0.22	0.10	0.24	0.36	0.71	0.45	0.14	0.13

*Removed from mean tally for EVFlowNet, as this sequence is part of the training set.

References

1. Mohammed Mutlaq Almatrafi and Keigo Hirakawa. DAViS camera optical flow. *IEEE Trans. Comput. Imaging*, pages 1–11, 2019.
2. Patrick Bardow, Andrew J. Davison, and Stefan Leutenegger. Simultaneous optical flow and intensity estimation from an event camera. In *IEEE Conf. Comput. Vis. Pattern Recog. (CVPR)*, pages 884–892, 2016.
3. Ryad Benosman, Charles Clercq, Xavier Lagorce, Sio-Hoi Ieng, and Chiara Bartolozzi. Event-based visual flow. *IEEE Trans. Neural Netw. Learn. Syst.*, 25(2):407–417, 2014.
4. Ryad Benosman, Sio-Hoi Ieng, Charles Clercq, Chiara Bartolozzi, and Mandyam Srinivasan. Asynchronous frameless event-based optical flow. *Neural Netw.*, 27:32–37, 2012.
5. Christian Brandli, Raphael Berner, Minhao Yang, Shih-Chii Liu, and Tobi Delbrück. A 240x180 130dB 3us latency global shutter spatiotemporal vision sensor. *IEEE J. Solid-State Circuits*, 49(10):2333–2341, 2014.
6. Tobias Brosch, Stephan Tschechne, and Heiko Neumann. On event-based optical flow detection. *Front. Neurosci.*, 9, Apr. 2015.
7. Alexey Dosovitskiy, Philipp Fischer, Eddy Ilg, Philip Häusser, Caner Hazırbaş, Vladimir Golkov, Patrick van der Smagt, Daniel Cremers, and Thomas Brox. FlowNet: Learning optical flow with convolutional networks. In *Int. Conf. Comput. Vis. (ICCV)*, pages 2758–2766, 2015.
8. Guillermo Gallego, Tobi Delbrück, Garrick Orchard, Chiara Bartolozzi, Brian Taba, Andrea Censi, Stefan Leutenegger, Andrew Davison, Jörg Conradt, Kostas Daniilidis, and Davide Scaramuzza. Event-based vision: A survey. *arXiv e-prints*, abs/1904.08405, 2019.
9. Guillermo Gallego, Mathias Gehrig, and Davide Scaramuzza. Focus is all you need: Loss functions for event-based vision. In *IEEE Conf. Comput. Vis. Pattern Recog. (CVPR)*, 2019.
10. Guillermo Gallego, Henri Rebecq, and Davide Scaramuzza. A unifying contrast maximization framework for event cameras, with applications to motion, depth, and optical flow estimation. In *IEEE Conf. Comput. Vis. Pattern Recog. (CVPR)*, pages 3867–3876, 2018.
11. Guillermo Gallego and Davide Scaramuzza. Accurate angular velocity estimation with an event camera. *IEEE Robot. Autom. Lett.*, 2(2):632–639, 2017.
12. Daniel Gehrig, Antonio Loquercio, Konstantinos G. Derpanis, and Davide Scaramuzza. End-to-end learning of representations for asynchronous event-based data. In *Int. Conf. Comput. Vis. (ICCV)*, 2019.
13. Yu Jason, Harley Adam, and Derpanis Konstantinos. Back to basics: Unsupervised learning of optical flow via brightness constancy and motion smoothness. 2016.
14. Hanme Kim, Ankur Handa, Ryad Benosman, Sio-Hoi Ieng, and Andrew J. Davison. Simultaneous mosaicing and tracking with an event camera. In *British Mach. Vis. Conf. (BMVC)*, 2014.
15. Hanme Kim, Stefan Leutenegger, and Andrew J. Davison. Real-time 3D reconstruction and 6-Dof tracking with an event camera. In *Eur. Conf. Comput. Vis. (ECCV)*, pages 349–364, 2016.
16. Wei-Sheng Lai, Jia-Bin Huang, Oliver Wang, Eli Shechtman, Ersin Yumer, and Ming-Hsuan Yang. Learning blind video temporal consistency. In *Eur. Conf. Comput. Vis. (ECCV)*, 2018.
17. Jun Haeng Lee, Tobi Delbrück, and Michael Pfeiffer. Training deep spiking neural networks using backpropagation. *Front. Neurosci.*, 10:508, 2016.
18. Patrick Lichtsteiner, Christoph Posch, and Tobi Delbrück. A 128×128 120 dB $15 \mu\text{s}$ latency asynchronous temporal contrast vision sensor. *IEEE J. Solid-State Circuits*, 43(2):566–576, 2008.
19. Tsung-Yi Lin, Michael Maire, Serge J. Belongie, Lubomir D. Bourdev, Ross B. Girshick, James Hays, Pietro Perona, Deva Ramanan, Piotr Dollár, and C. Lawrence Zitnick. Microsoft COCO: Common objects in context. In *Eur. Conf. Comput. Vis. (ECCV)*, 2014.

20. Min Liu and Tobi Delbruck. Adaptive time-slice block-matching optical flow algorithm for dynamic vision sensors. In *British Mach. Vis. Conf. (BMVC)*, 2018.
21. Ana I. Maqueda, Antonio Loquercio, Guillermo Gallego, Narciso García, and Davide Scaramuzza. Event-based vision meets deep learning on steering prediction for self-driving cars. In *IEEE Conf. Comput. Vis. Pattern Recog. (CVPR)*, pages 5419–5427, 2018.
22. Elias Mueggler, Christian Forster, Nathan Baumli, Guillermo Gallego, and Davide Scaramuzza. Lifetime estimation of events from dynamic vision sensors. In *IEEE Int. Conf. Robot. Autom. (ICRA)*, pages 4874–4881, 2015.
23. Elias Mueggler, Henri Rebecq, Guillermo Gallego, Tobi Delbruck, and Davide Scaramuzza. The event-camera dataset and simulator: Event-based data for pose estimation, visual odometry, and SLAM. *Int. J. Robot. Research*, 36(2):142–149, 2017.
24. Garrick Orchard, Cedric Meyer, Ralph Etienne-Cummings, Christoph Posch, Nitish Thakor, and Ryad Benosman. HFirst: A temporal approach to object recognition. *IEEE Trans. Pattern Anal. Mach. Intell.*, 37(10):2028–2040, 2015.
25. José A. Perez-Carrasco, Bo Zhao, Carmen Serrano, Begoña Acha, Teresa Serrano-Gotarredona, Shouchun Chen, and Bernabé Linares-Barranco. Mapping from frame-driven to frame-free event-driven vision systems by low-rate rate coding and coincidence processing—application to feedforward ConvNets. *IEEE Trans. Pattern Anal. Mach. Intell.*, 35(11):2706–2719, Nov. 2013.
26. Henri Rebecq, Daniel Gehrig, and Davide Scaramuzza. ESIM: an open event camera simulator. In *Conf. on Robot. Learning (CoRL)*, 2018.
27. Henri Rebecq, René Ranftl, Vladlen Koltun, and Davide Scaramuzza. Events-to-video: Bringing modern computer vision to event cameras. In *IEEE Conf. Comput. Vis. Pattern Recog. (CVPR)*, 2019.
28. Henri Rebecq, René Ranftl, Vladlen Koltun, and Davide Scaramuzza. High speed and high dynamic range video with an event camera. *IEEE Trans. Pattern Anal. Mach. Intell.*, 2020.
29. Henri Rebecq, René Ranftl, Vladlen Koltun, and Davide Scaramuzza. High speed and high dynamic range video with an event camera. *IEEE Trans. Pattern Anal. Mach. Intell.*, 2020.
30. Christian Reinbacher, Gottfried Gruber, and Thomas Pock. Real-time intensity-image reconstruction for event cameras using manifold regularisation. In *British Mach. Vis. Conf. (BMVC)*, 2016.
31. Cedric Scheerlinck, Nick Barnes, and Robert Mahony. Continuous-time intensity estimation using event cameras. In *Asian Conf. Comput. Vis. (ACCV)*, 2018.
32. Cedric Scheerlinck, Nick Barnes, and Robert Mahony. Asynchronous spatial image convolutions for event cameras. *IEEE Robot. Autom. Lett.*, 4(2):816–822, Apr. 2019.
33. Cedric Scheerlinck, Henri Rebecq, Daniel Gehrig, Nick Barnes, Robert Mahony, and Davide Scaramuzza. Fast image reconstruction with an event camera. In *IEEE Winter Conf. Appl. Comput. Vis. (WACV)*, 2020.
34. Cedric Scheerlinck, Henri Rebecq, Timo Stoffregen, Nick Barnes, Robert Mahony, and Davide Scaramuzza. CED: color event camera dataset. In *IEEE Conf. Comput. Vis. Pattern Recog. Workshops (CVPRW)*, 2019.
35. Amos Sironi, Manuele Brambilla, Nicolas Bourdis, Xavier Lagorce, and Ryad Benosman. HATS: Histograms of averaged time surfaces for robust event-based object classification. In *IEEE Conf. Comput. Vis. Pattern Recog. (CVPR)*, pages 1731–1740, 2018.
36. Timo Stoffregen, Guillermo Gallego, Tom Drummond, Lindsay Kleeman, and Davide Scaramuzza. Event-based motion segmentation by motion compensation. In *Int. Conf. Comput. Vis. (ICCV)*, 2019.
37. Timo Stoffregen and Lindsay Kleeman. Simultaneous optical flow and segmentation (SO-FAS) using Dynamic Vision Sensor. In *Australasian Conf. Robot. Autom. (ACRA)*, 2017.
38. Timo Stoffregen and Lindsay Kleeman. Event cameras, contrast maximization and reward functions: an analysis. In *IEEE Conf. Comput. Vis. Pattern Recog. (CVPR)*, 2019.

39. Zhou Wang, Alan C. Bovik, Hamid R. Sheikh, and Eero P. Simoncelli. Image quality assessment: From error visibility to structural similarity. *IEEE Trans. Image Process.*, 13(4):600–612, Apr. 2004.
40. Chengxi Ye, Anton Mitrokhin, Chethan Parameshwara, Cornelia Fermüller, James A. Yorke, and Yiannis Aloimonos. Unsupervised learning of dense optical flow and depth from sparse event data. *arXiv e-prints*, 2019.
41. Linguang Zhang and Szymon Rusinkiewicz. Learning to detect features in texture images. In *IEEE Conf. Comput. Vis. Pattern Recog. (CVPR)*, 2018.
42. Richard Zhang, Phillip Isola, Alexei A. Efros, Eli Shechtman, and Oliver Wang. The unreasonable effectiveness of deep features as a perceptual metric. In *IEEE Conf. Comput. Vis. Pattern Recog. (CVPR)*, 2018.
43. Alex Zihao Zhu, Dinesh Thakur, Tolga Ozaslan, Bernd Pfommer, Vijay Kumar, and Kostas Daniilidis. The multivehicle stereo event camera dataset: An event camera dataset for 3D perception. *IEEE Robot. Autom. Lett.*, 3(3):2032–2039, July 2018.
44. Alex Zihao Zhu, Liangzhe Yuan, Kenneth Chaney, and Kostas Daniilidis. EV-FlowNet: Self-supervised optical flow estimation for event-based cameras. In *Robotics: Science and Systems (RSS)*, 2018.
45. Alex Zihao Zhu, Liangzhe Yuan, Kenneth Chaney, and Kostas Daniilidis. Unsupervised event-based learning of optical flow, depth, and egomotion. In *IEEE Conf. Comput. Vis. Pattern Recog. (CVPR)*, 2019.

6 Supplementary Materials

6.1 Voxel Generation

Several methods can be used when generating voxel grids from the event stream. The two most natural are fixed rate and fixed events. In fixed rate, voxels are formed from t wide slices of the event stream, endowing the resulting inference with a fixed frame rate.

In fixed rate, to form the voxel grid V with B bins V_B given a time range Δ_T and thus N events $e_i = \{x_i, y_i, t_i, p_i\}_{i=0, \dots, N}$ such that $t_N - t_0 = \Delta_T$, each event distributes its polarity to the nearest bins through a bilinear interpolation

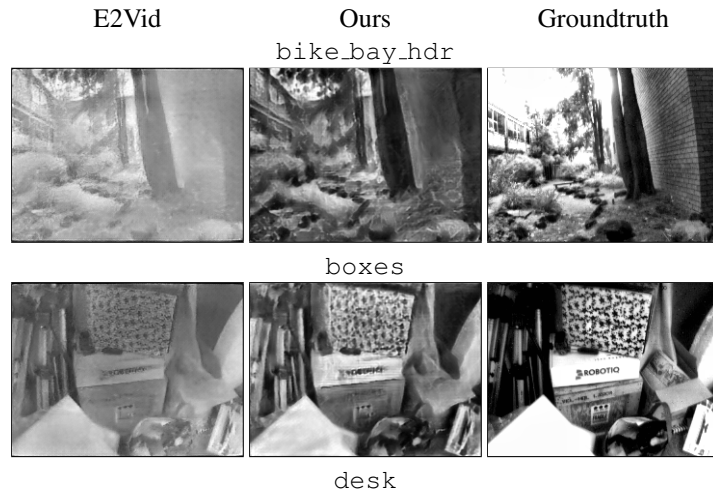
$$V_{k \in [0, B-1]} = \sum_{i=0}^N p_i \max(0, 1 - |t_i^* - k|) \quad (3)$$

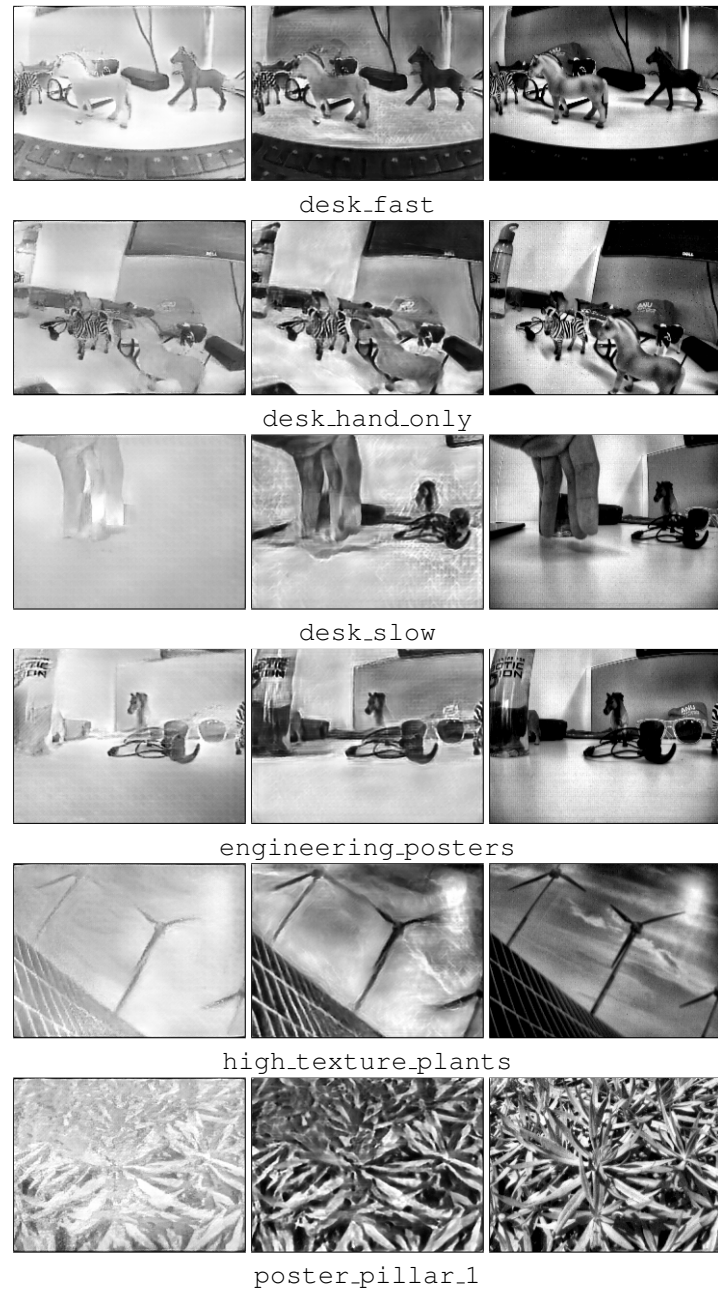
where t_i^* is the timestamp normalized to the range $[0, B-1]$ via $t_i^* = \frac{t_i - t_0}{\Delta_T}(B-1)$ and the bins are evenly spaced over the range $[t_0, t_N]$.

This has the downside that inference cannot adapt to changing scene dynamics and the event camera essentially becomes a conventional camera. Further, parts of the scene that cause many events, may generate values in the voxel grid that lie far outside the networks experience.

In the fixed-events method, rather than choosing N based on Δ_T , N is chosen according to a fixed Δ_T . Fixed rate has the downside that if the camera receives few events, either because the scene has little texture or the motion is slow, the inference rate can drop to become very slow. However, this method allows matching the value N to the average value \bar{N} from the training set during inference, making the task easier for the network. The average events per voxel in our training set is 0.0564.

6.2 Additional Qualitative Results







poster_pillar_2



reflective_materials



slow_and_fast_desk_scene



slow_hand



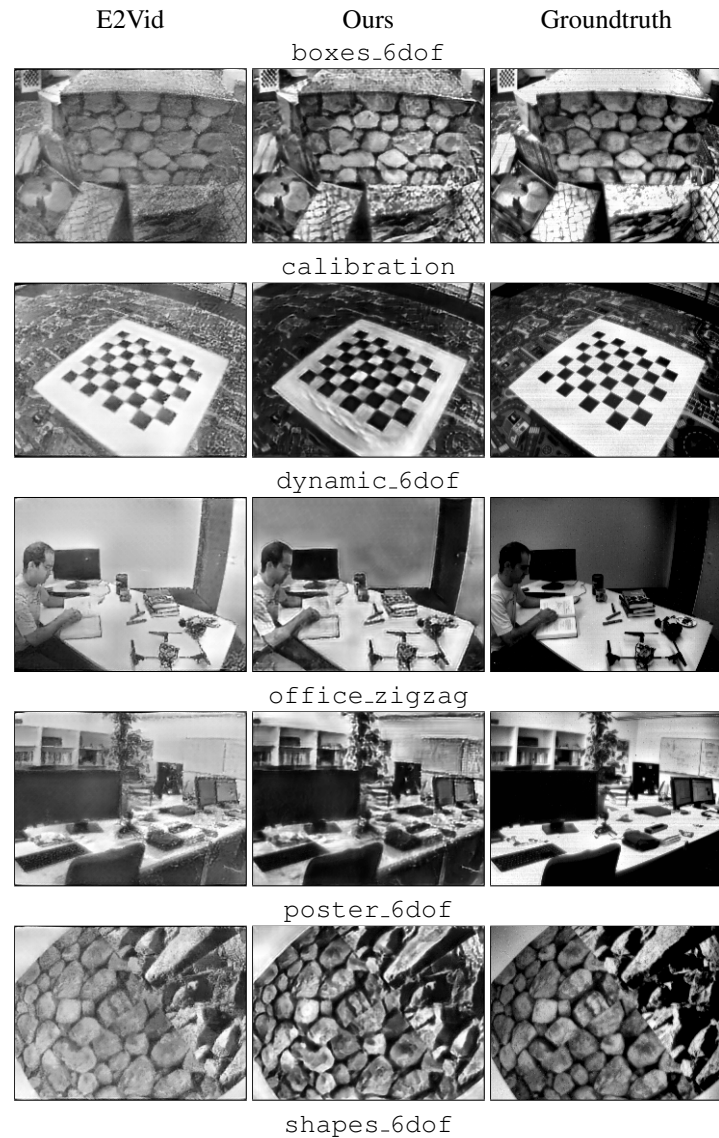
still_life



tearoom



Table 7: Qualitative results for HQFD. Random selection, not cherry picked.



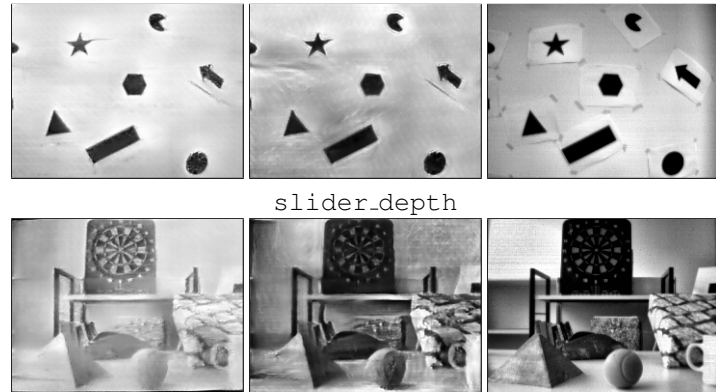


Table 8: Qualitative results for IJRR. Random selection, not cherry picked.





Table 9: Qualitative results for MVSEC. Random selection, not cherry picked.

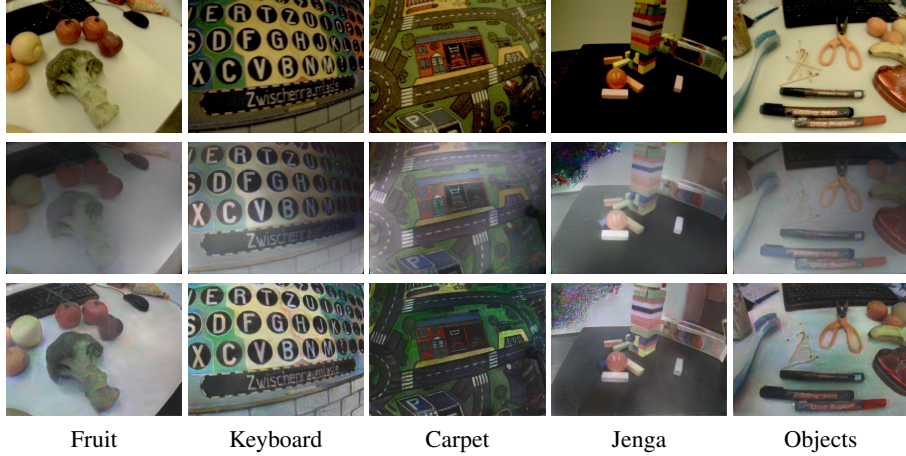


Fig. 5: Results of our method vs E2Vid [27] on the Color Event Dataset [34]. APS frames top row, E2Vid middle row, ours bottom row. As a matter of interest, the Jenga sequence shows a region of the scene where there is only blank wall, so few events have been generated, resulting in the peculiar artifacts seen in the top left corner.

6.3 CTs extended

As outlined in Sec. 3, we propose several methods for estimating the CTs for a given event-based dataset. In total, we tried three different methods:

- Creating a simulator scene with similar texture and range of motions as the real sequence and adjusting the CTs until the $\frac{\text{events}}{\text{pix} \cdot \text{s}}$ match.

- Simulating events from the APS frames (if they are available) and adjusting the CTs until the $\frac{\text{events}}{\text{pix}\cdot\text{s}}$ match the real sequence.
- Creating a calibration scene in the simulator, recording this scene on-screen and adjusting the CT of the event camera to match the $\frac{\text{events}}{\text{pix}\cdot\text{s}}$ of the simulation.

We describe the first two approaches in the main paper. These approaches indicate CTs of approximately 0.3 and 0.75 for IJRR and MVSEC respectively.

We also produced a calibration sequence in an attempt to match the simulator to our particular DAVIS 240C at default settings. For this, we moved a checkerboard across the image plane in ESIM, using various CTs. The scene was played on a high-refresh screen and recorded by our DAVIS. The resulting event-rate for each sequence, shown in Tab. 10, suggest a $\text{CT} \approx 0.5$ to match the camera to the simulator. This is however in conflict with the $\frac{\text{events}}{\text{pix}\cdot\text{s}}$ (8.2) of the real sequences compared to the $\frac{\text{events}}{\text{pix}\cdot\text{s}}$ of the best training data CT (19.6). In other words, there seems to be a mismatch for this method of calibration, perhaps stemming from a difference in recording events from real scenes to recording scenes from a screen as was done for the checkerboard calibration sequence.

Table 10: Comparison of the $\frac{\text{events}}{\text{pix}\cdot\text{s}}$ for simulated sequences at various CT settings with the $\frac{\text{events}}{\text{pix}\cdot\text{s}}$ of a real calibration sequence. The sequence consists of a checkerboard in motion. The same sequence is also recorded by a real event camera (DAVIS 240C) using default bias settings. The result suggests that a CT value around 0.5 would be appropriate to match the simulator to the real camera.

Data CT	0.2	0.5	0.75	1.0	1.5	Real
$\frac{\text{events}}{\text{pix}\cdot\text{s}}$	26.5	19.6	16.2	10.8	7.2	8.2
LPIPS	0.289	0.285	0.289	0.311	0.316	-

6.4 Sequence Cuts

Since the frames accompanying the events in the commonly used MVSEC and IJRR datasets are of low quality, we only evaluate on select sequences and for select cuts of those sequences. These cuts are enumerated in Tab. 11.

6.5 FireNet

Scheerlinck *et al.* [33] propose a lightweight network architecture for fast image reconstruction with an event camera (FireNet) that has 99.6 % fewer parameters than E2VID [29] while achieving similar accuracy on IJRR [23]. We retrain FireNet using our method and evaluate the original (FireNet) vs. retrained (FireNet+) on IJRR, MVSEC and HQF (Tab. 12). FireNet+ performs better on HQF and MVSEC though worse on IJRR. One possible explanation is that the limited capacity of a smaller network limits generalizability over a wider distribution of data, and the original FireNet

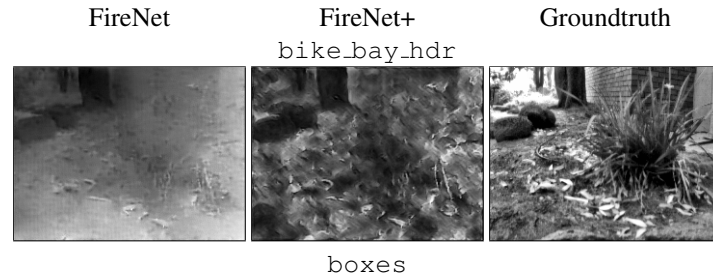
Table 11: Start and end times for the sequences in IJRR and MVSEC which we present validation statistics on. While both IJRR and MVSEC contain more sequences than the ones listed, those not included had very low quality accompanying frames (see Fig. 3).

IJRR			MVSEC		
Sequence	Start [s]	End [s]	Sequence [s]	Start [s]	End [s]
boxes_6dof	5.0	20.0	indoor_flying1	10.0	70.0
calibration	5.0	20.0	indoor_flying2	10.0	70.0
dynamic_6dof	5.0	20.0	indoor_flying3	10.0	70.0
office_zigzag	5.0	12.0	indoor_flying4	10.0	19.8
poster_6dof	5.0	20.0	outdoor_day1	0.0	60.0
shapes_6dof	5.0	20.0	outdoor_day2	100.0	160.0
slider_depth	1.0	2.5			

overfits to data similar to IJRR, namely low CTs. If our hypothesis is correct, it presents an additional disadvantage to small networks for event cameras. Comprehensive evaluation (HQF + IJRR + MVSEC) reveals bigger performance gap between FireNet (Tab. 12) and E2Vid (Tab. 6) architectures than shown in [33] (IJRR only). Qualitatively (Fig. 13), FireNet+ looks noisier in textureless regions, while FireNet produces lower contrast images.

Table 12: Mean MSE, SSIM [39] and LPIPS [42] on our HQF dataset, IJRR [23] and MVSEC [43], for original FireNet vs. retrained with our method (FireNet+).

Model	HQF			IJRR			MVSEC		
	MSE	SSIM	LPIPS	MSE	SSIM	LPIPS	MSE	SSIM	LPIPS
FireNet	0.065	0.481	0.415	0.062	0.573	0.290	0.173	0.290	0.640
FireNet+	0.052	0.473	0.359	0.057	0.508	0.317	0.166	0.269	0.562



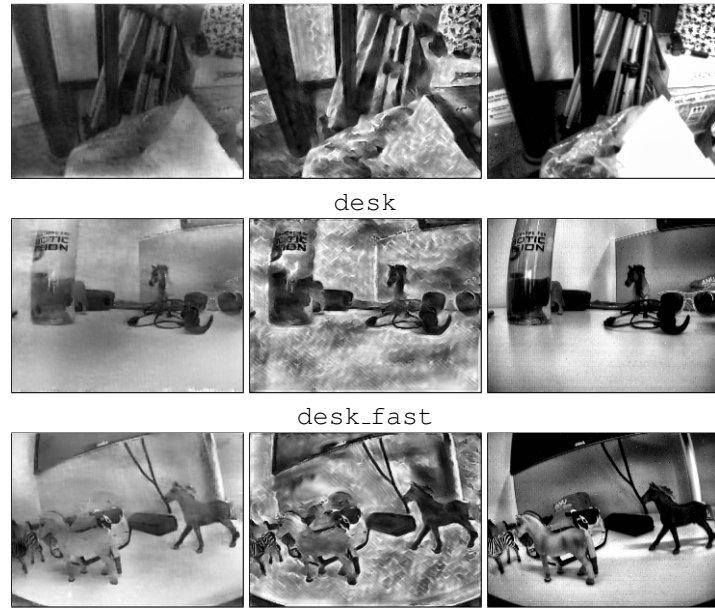


Table 13: Qualitative results for HQFD. Random selection, not cherry picked.

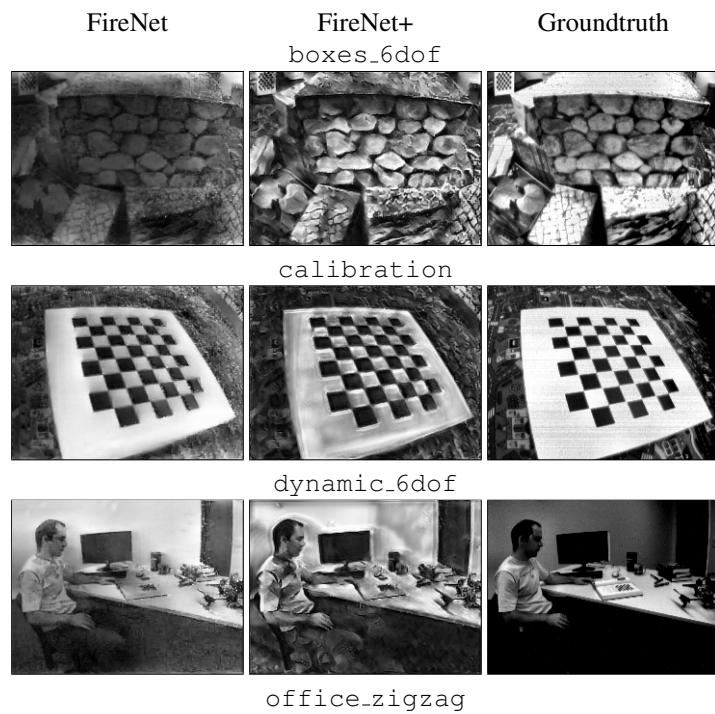




Table 14: Qualitative results for IJRR. Random selection, not cherry picked.

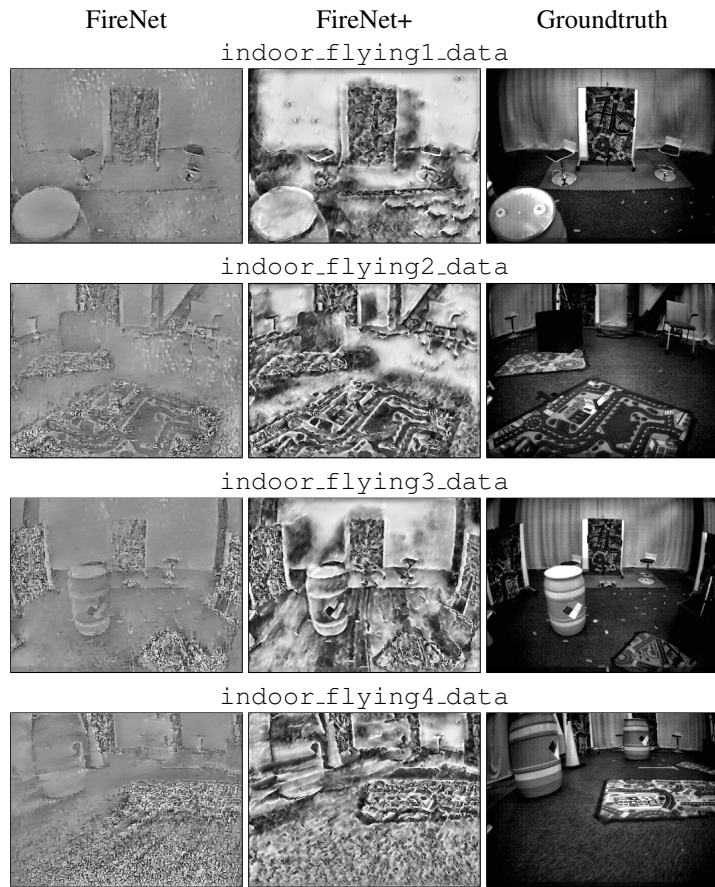


Table 15: Qualitative results for MVSEC. Random selection, not cherry picked.